Electronic Research Archive

http://www.aimspress.com/journal/era

ERA, 31(6): 3322–3342.
DOI: 10.3934/era.2023168
Received: 07 February 2023
Revised: 26 March 2023
Accepted: 03 April 2023
Published: 12 April 2023

Research article

A hybrid method for the interior inverse scattering problem

Yujie Wang, Enxi Zheng*and Wenyan Wang

School of Science, Dalian Maritime University, No. 1 of Linghai Road, Dalian 116026, Liaoning, China

* **Correspondence:** Email: enxizheng2003@dlmu.edu.cn.

Abstract: In this paper, the interior inverse scattering problem of a cavity is considered. By use of a general boundary condition, we can reconstruct the shape of the cavity without a priori information of the boundary condition type. The method of fundamental solutions (MFS) with regularization is formulated for solving the scattered field and its normal derivative on the cavity boundary. Newton's method is employed to reconstruct the cavity boundary by satisfying the general boundary condition. This hybrid method copes with the ill-posedness of the inverse problem in the MFS step and deals with the nonlinearity in the Newton's step. Some computational examples are presented to demonstrate the effectiveness of our method.

Keywords: hybrid method; inverse cavity problem; method of fundamental solutions; interior scattering; unknown boundary condition

1. Introduction

Inverse scattering problems play an important role in many areas, such as radar detection, medical imaging and non-destructive testing [1]. The classic inverse scattering problem is usually viewed as an exterior problem. For example, the bounded obstacle is illuminated by an incident plane wave, and the shape of the obstacle can be reconstructed via the measured far-field data [1–3]. In recent decades, interior inverse scattering problems have also attracted the attention of many researchers due to their applications in industry. In such interior problems, the scatterer is always described as a closed cavity. The sources and receivers are placed inside the cavity to test its structural integrity based on the scattered waves received [4]. In our paper, we define the cavity by a bounded, simply connected domain $D \subset \mathbb{R}^2$ with a Lipschitz boundary ∂D. The point sources and the receivers are placed on a closed curve C inside the cavity D (see Figure 1). We try to reconstruct the cavity boundary ∂D from the scattered waves measured on C via a hybrid method without knowing the boundary condition.

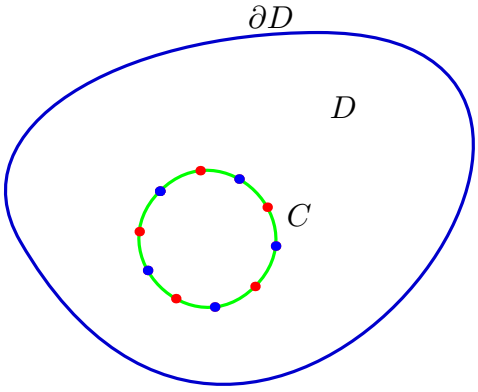

Figure 1. Interior scattering problem of a cavity.

In comparison with the exterior scattering problem, the interior scattering problem is more complicated due to the repeated reflections of the trapped scattered waves in the cavity. Some numerical methods have been studied for interior inverse scattering problems. In [5], Qin and Colton proved the uniqueness of this interior problem with the Dirichlet boundary condition and proposed a modification of the linear sampling method to reconstruct the shape of the cavity. They also developed this method for the case of the impedance boundary condition [6]. In [7], the authors used the linear sampling method to solve the interior inverse electromagnetic scattering problem, and, recently, this method has been extended to the inhomogeneous case [8]. Many other numerical methods are also available for interior inverse scattering problems, such as the integral equation method [9], decomposition method [10], regularized Newton's iterative method [11], factorization method [12, 13], Bayesian method [14], reciprocity gap method [15], direct imaging method [16] and so on. The interior inverse scattering problem for a two-layered cavity was considered in [17], and the authors used the Bayesian method to reconstruct the interface. Interior inverse scattering problems with different physical backgrounds have also been studied. For example, in [18], the shape of an elastic cavity was reconstructed, and, in [19, 20], a partially coated cavity with mixed boundary conditions was studied. Recently, machine learning approaches for solving inverse scattering problems have become popular [21, 22]. In [23], the authors have also proposed a neural network method for inverse scattering problems of impenetrable cavities.

As stated above, many numerical methods have been proposed for the interior inverse scattering problem. Most of them, for example, the regularized Newton method and the decomposition method, need to know the boundary condition as a priori information. However, in some practical applications, the physical properties of the cavity are unknown. As a result, the type of boundary condition in the mathematical model of the interior inverse scattering problem is unknown. Motivated by the idea in [24], we introduce a general boundary condition in our model instead of the traditional Dirichlet or impedance boundary condition. Then, we propose a hybrid method by coupling the method of fundamental solutions (MFS) and the Newton's iterative method. By use of the general boundary condition introduced in [24], we can reconstruct the shape of a cavity without a priori knowledge concerning the size and physical properties of the cavity. Similar to the hybrid methods used in [24–27], we need to reconstruct the cavity boundary that satisfies the general boundary condition. This is a nonlinear problem, and we cope with it via the Newton's method. The general boundary condition consists of the real parts and imaginary parts of the total field and its normal derivative. Therefore,

in each iteration of the Newton's method, we try to obtain the total field and its normal derivative on the approximated cavity boundary from the scattered field measured on C by the MFS. Because the resulting system of equations produced by the MFS is ill-posed, we adopt the regularization technique. The advantage of the hybrid method is that it obtains a good compromise between numerical accuracy, computational costs and the amount of required data (one incident wave is sufficient). In our hybrid method, we use the regularized MFS instead of the integral equation method in the first step, which makes the method simpler and easier to code.

The outline of this paper is as follows. In Section 2, we provide the formulation of the interior inverse scattering problem and prove the uniqueness result. In Section 3, we present the hybrid method and the general boundary condition used in our algorithm. In Section 4, some numerical examples are presented to demonstrate the effectiveness of our method. In Section 5, we conclude the paper and present some research directions for our future work.

2. Formulation of the problem

In this paper, we consider a transverse magnetic (TM) polarized time-harmonic electric dipole located inside an infinite cylinder. Let the cross section of the cylinder $D \subset \mathbb{R}^2$ be a simply connected domain with a Lipschitz boundary ∂D. The point sources and the observational points are all located on curve C inside D (see Figure 1). Then, the scattered field u^s of the interior scattering problem satisfies the following equation:

$$\Delta u^s + k^2 u^s = 0 \quad \text{in } D, \tag{2.1}$$

where $k > 0$ is the wave number. Suppose that u^i is the incident field given by

$$u^i(\boldsymbol{x}) = \Phi(\boldsymbol{x}, \boldsymbol{d}) = \frac{\mathrm{i}}{4} H_0^{(1)}(k|\boldsymbol{x} - \boldsymbol{d}|).$$

Here, $\mathrm{i} = \sqrt{-1}$, $\boldsymbol{d}$ is the location of the source point on C and $\Phi(\boldsymbol{x}, \boldsymbol{d})$ is the fundamental solution of the two-dimensional Helmholtz equation. The total field $u = u^i + u^s$ satisfies the following boundary condition:

$$\mathcal{B}u = 0, \quad \text{on } \partial D, \tag{2.2}$$

where $\mathcal{B}$ is a linear operator defined by

$$\mathcal{B} = I, \quad \text{for Dirichlet boundary condition,} \tag{2.3}$$

$$\mathcal{B} = \frac{\partial}{\partial \boldsymbol{\nu}}, \quad \text{for Neumann boundary condition,} \tag{2.4}$$

$$\mathcal{B} = \frac{\partial}{\partial \boldsymbol{\nu}} + \mathrm{i}\lambda(\boldsymbol{x})I, \quad \text{for impedance boundary condition.} \tag{2.5}$$

Here, $\lambda(\boldsymbol{x}) \geqslant 0$ is a real-valued impedance function on ∂D and $\lambda(\boldsymbol{x}) \in C(\partial D)$. $\boldsymbol{\nu}$ is the unit outward normal vector with respect to ∂D. Actually, the Neumann boundary condition (2.4) can be viewed as the impedance boundary condition (2.5) with an impedance of $\lambda = 0$.

For the direct problem, we solve the scattered field u^s from Eq (2.1) and the boundary condition (2.2). For the inverse problem, we reconstruct the geometry of the cavity D and the impedance function $\lambda(\boldsymbol{x})$ in the case with an impedance boundary condition from the measured scattered fields u^s. In this

paper, we consider the interior inverse scattering problem without knowing the physical properties of the cavity D. Because the boundary condition is related to the physical properties of D, it is usually difficult to obtain the boundary condition as a priori information. Therefore, we try to reconstruct the geometry of the interior cavity from the scattered field u^s on curve C without knowing whether the boundary operator $\mathcal{B}$ is (2.3), (2.4) or (2.5). To this end, we introduce a general boundary condition in the next section. Before we illustrate the hybrid method for solving the interior inverse scattering problem, we focus on the uniqueness of our problem. Motivated by the uniqueness proofs of Theorem 2.1 in [19] and Theorem 2.2 in [28], we present the next theorem. Throughout the paper, we assume that k^2 is not a Dirichlet eigenvalue for $-\Delta$ in the interior of C.

Theorem 1. *Assume that D_1, D_2 are two cavities with boundary conditions $\mathcal{B}_1, \mathcal{B}_2$, respectively, such that the scattered fields coincide on C for all source points located on C and a fixed wave number. Here, $\mathcal{B}_1, \mathcal{B}_2$ are assumed to be one of the boundary operators defined by (2.3), (2.4) or (2.5). Then, $D_1 = D_2$ and $\mathcal{B}_1 = \mathcal{B}_2$.*

Proof. The proof is divided into three steps.

In step 1, we prove the uniqueness of D, that is, $D_1 = D_2$. This part of the proof is similar to the proof of Theorem 2.1 in [19].

In step 2, we prove the uniqueness of the boundary condition type. Let $u_1^s(\boldsymbol{x}, \boldsymbol{d})$ and $u_2^s(\boldsymbol{x}, \boldsymbol{d})$ be the scattered fields of cavities D_1 and D_2 for one source point located at $\boldsymbol{d} \in C$. From the assumption, $u_1^s = u_2^s$ for all $\boldsymbol{x}$ on C. Then, from the proof of Theorem 2.1 in [19], the total fields $u_1(\boldsymbol{x}, \boldsymbol{d}) = u^i + u_1^s = u^i + u_2^s = u_2(\boldsymbol{x}, \boldsymbol{d})$ in $D := D_1 = D_2$, which is proven in step 1. For simplicity, we use u instead of u_1 and u_2. If the boundary conditions of the two cavities are different, without loss of generality, we can assume that the total field $u = u^i + u^s = 0$ on ∂D_1 and $\frac{\partial u}{\partial \boldsymbol{\nu}} + \mathrm{i}\lambda(\boldsymbol{x})u = 0$ on ∂D_2. Since $D = D_1 = D_2$, we have that $\frac{\partial u}{\partial \boldsymbol{\nu}} = 0$ on ∂D. Utilizing Holmgren's theorem, we know that $u(\boldsymbol{x}) = 0$ for all $\boldsymbol{x} \in D \backslash \{\boldsymbol{d}\}$, noticing that the total field u is analytic in D except at point $\boldsymbol{d}$. Therefore, the scattered field $u_1^s(\boldsymbol{x}, \boldsymbol{d}) = -\Phi(\boldsymbol{x}, \boldsymbol{d})$ for $\boldsymbol{x} \neq \boldsymbol{d}$. This means that the scattered field blows up when $\boldsymbol{x} \longrightarrow \boldsymbol{d}$. This is a contradiction. Thus, the types of boundary conditions are the same for D_1 and D_2.

In step 3, we prove the uniqueness of λ for the impedance boundary condition. From step 2, we have that $u_1 = u_2$ in D. Then,

$$u_1 = u_2, \quad \frac{\partial u_1}{\partial \boldsymbol{\nu}} = \frac{\partial u_2}{\partial \boldsymbol{\nu}} \quad on \quad \partial D.$$

We subtract the impedance boundary conditions

$$\frac{\partial u_1}{\partial \boldsymbol{\nu}} + \mathrm{i}\lambda_1 u_1 = 0, \quad \frac{\partial u_2}{\partial \boldsymbol{\nu}} + \mathrm{i}\lambda_2 u_2 = 0.$$

Then, we obtain

$$(\lambda_1 - \lambda_2)u = 0, \quad on \quad \partial D.$$

Assume $\lambda_1 \neq \lambda_2$ at a point $\boldsymbol{x}_0$ on ∂D; then, there exists a neighborhood of $\boldsymbol{x}_0$ such that $\lambda_1 \neq \lambda_2$ on $O(\boldsymbol{x}_0, \epsilon) \cap \partial D$. This means that $u = 0$ on $O(\boldsymbol{x}_0, \epsilon) \cap \partial D$, and, from the impedance boundary condition, $\frac{\partial u}{\partial \boldsymbol{\nu}} = 0$. Similar to the proof in step 2, we obtain $u = 0$ for all $\boldsymbol{x} \in D \backslash \{\boldsymbol{d}\}$ by use of Holmgren's theorem. Therefore, we can obtain the contradiction in the same way as in step 2.

Remark 1. *The above uniqueness result is obtained from the scattered fields on C for all source points located on C. Actually, in the numerical experiments conducted in Section 4, we can reconstruct*

the shape of the cavity with just one point source incidence. Notably, better reconstructions can be obtained with more source points.

3. The hybrid method

In this section, we propose a general boundary condition and a hybrid method for addressing the interior inverse scattering problem.

3.1. The general boundary condition

As stated above, there are three types of boundary conditions and the Neumann condition can be viewed as the impedance condition with $\lambda = 0$. Now, we introduce the general boundary condition from [24], which is defined as follows:

$$G(u) := \mathcal{R}\left(\frac{\partial u}{\partial \boldsymbol{\nu}}\right)\mathcal{R}(u) + \mathcal{I}\left(\frac{\partial u}{\partial \boldsymbol{\nu}}\right)\mathcal{I}(u) = 0, \quad \text{on } \partial D, \tag{3.1}$$

where $\mathcal{R}(u)$ represents the real part of u and $\mathcal{I}(u)$ represents the imaginary part of u. The relationship between the above general boundary condition and the usual boundary conditions is stated in the following theorem.

Theorem 2. *Assume that D is a bounded cavity with a C^2 continuous boundary ∂D, the function $u \in C^2(D) \cap C(\bar{D})$ and $u \neq 0$ everywhere on ∂D if $u \equiv 0$ is not true on ∂D. Then, u satisfies the general boundary condition*

$$G(u) = 0 \quad \text{on } \partial D$$

if and only if u satisfies the Dirichlet boundary condition $u = 0$ or the impedance boundary condition $\partial u/\partial \boldsymbol{\nu} + \mathrm{i}\lambda u = 0$ on ∂D.

Proof. The proof of this theorem is similar to the proof of Theorem 2.1 in [24]. Because this general boundary condition is a key part of our hybrid method, we repeat the proof as follows.

First, we prove the sufficiency. If $u = 0$ on ∂D, then $G(u) = 0$ on ∂D. If $\partial u/\partial \boldsymbol{\nu} + \mathrm{i}\lambda u = 0$ on ∂D, we have

$$\left(\mathcal{R}\left(\frac{\partial u}{\partial \boldsymbol{\nu}}\right) - \lambda\mathcal{I}(u)\right) + \mathrm{i}\left(\mathcal{I}\left(\frac{\partial u}{\partial \boldsymbol{\nu}}\right) + \lambda\mathcal{R}(u)\right) = 0, \quad \text{on } \partial D.$$

Therefore,

$$\mathcal{R}\left(\frac{\partial u}{\partial \boldsymbol{\nu}}\right) = \lambda\mathcal{I}(u), \ \mathcal{I}\left(\frac{\partial u}{\partial \boldsymbol{\nu}}\right) = -\lambda\mathcal{R}(u) \quad \text{on } \partial D.$$

Obviously, if $\lambda = 0$, $\partial u/\partial \boldsymbol{\nu} = 0$ on ∂D. Thus, $G(u) = 0$. If $\lambda \neq 0$, multiply the above two equations, and we obtain

$$-\lambda\mathcal{R}(u)\mathcal{R}\left(\frac{\partial u}{\partial \boldsymbol{\nu}}\right) = \lambda\mathcal{I}(u)\mathcal{I}\left(\frac{\partial u}{\partial \boldsymbol{\nu}}\right) \quad \text{on } \partial D.$$

$$\mathcal{R}\left(\frac{\partial u}{\partial \boldsymbol{\nu}}\right)\mathcal{R}(u) + \mathcal{I}\left(\frac{\partial u}{\partial \boldsymbol{\nu}}\right)\mathcal{I}(u) = 0, \quad \text{on } \partial D.$$

Therefore, we obtain the general boundary condition $G(u) = 0$ on ∂D for the impedance boundary condition.

Second, we prove the necessity. If $G(u) = 0$ on ∂D, we have that

$$\begin{aligned} & u\mathcal{R}\left(\frac{\partial u}{\partial \boldsymbol{\nu}}\right) - \mathrm{i}\mathcal{I}(u)\frac{\partial u}{\partial \boldsymbol{\nu}} \\ =& u\mathcal{R}\left(\frac{\partial u}{\partial \boldsymbol{\nu}}\right) - \mathrm{i}\mathcal{I}(u)\mathcal{R}\left(\frac{\partial u}{\partial \boldsymbol{\nu}}\right) + \mathcal{I}(u)\mathcal{I}\left(\frac{\partial u}{\partial \boldsymbol{\nu}}\right) \\ =& \mathcal{R}(u)\mathcal{R}\left(\frac{\partial u}{\partial \boldsymbol{\nu}}\right) + \mathrm{i}\mathcal{I}(u)\mathcal{R}\left(\frac{\partial u}{\partial \boldsymbol{\nu}}\right) - \mathrm{i}\mathcal{I}(u)\mathcal{R}\left(\frac{\partial u}{\partial \boldsymbol{\nu}}\right) + \mathcal{I}(u)\mathcal{I}\left(\frac{\partial u}{\partial \boldsymbol{\nu}}\right) \\ =& \mathcal{R}\left(\frac{\partial u}{\partial \boldsymbol{\nu}}\right)\mathcal{R}(u) + \mathcal{I}\left(\frac{\partial u}{\partial \boldsymbol{\nu}}\right)\mathcal{I}(u) \\ =& 0. \end{aligned} \tag{3.2}$$

Similarly, we obtain

$$u\mathcal{I}\left(\frac{\partial u}{\partial \boldsymbol{\nu}}\right) - \mathrm{i}\mathcal{R}(u)\frac{\partial u}{\partial \boldsymbol{\nu}} = 0 \quad \textit{on } \partial D. \tag{3.3}$$

Subtract (3.3)$\times\mathcal{R}(u)$ from (3.2)$\times\mathcal{I}(u)$

$$u\left(\mathcal{R}\left(\frac{\partial u}{\partial \boldsymbol{\nu}}\right)\mathcal{I}(u) - \mathcal{I}\left(\frac{\partial u}{\partial \boldsymbol{\nu}}\right)\mathcal{R}(u)\right) - \mathrm{i}((\mathcal{I}(u))^2 + (\mathcal{R}(u))^2)\frac{\partial u}{\partial \boldsymbol{\nu}} = 0.$$

From the above equation, we have that $u = 0$ or $\partial u/\partial \boldsymbol{\nu} + \mathrm{i}\lambda u = 0$ on ∂D, where λ is defined with the following form:

$$\lambda := \frac{\mathcal{R}\left(\frac{\partial u}{\partial \boldsymbol{\nu}}\right)\mathcal{I}(u) - \mathcal{I}\left(\frac{\partial u}{\partial \boldsymbol{\nu}}\right)\mathcal{R}(u)}{(\mathcal{I}(u))^2 + (\mathcal{R}(u))^2}. \tag{3.4}$$

3.2. Two steps of the hybrid method

Now, by using the above general boundary condition, we propose a hybrid method for the interior inverse scattering problem. First, we give the parametric form of the cavity boundary ∂D:

$$\boldsymbol{z}(t) = r(t)(\cos t, \sin t), \quad t \in [0, 2\pi], \tag{3.5}$$

where $r(t) = a_0 + \sum_{j=1}^{\infty}[a_j \cos(jt) + b_j \sin(jt)] > 0$. In numerical experiments, we truncate $r(t)$ by N_1 terms.

Next, we illustrate the main idea of the hybrid method, which consists of two steps. In the first step, we represent the total field trace u and its normal derivative $\frac{\partial u}{\partial \boldsymbol{\nu}}$ on ∂D by the MFS. After choosing N source points $\boldsymbol{y}_i$ on a closed curve S containing the cavity D,

$$u^s(\boldsymbol{x}) \approx \sum_{i=1}^{N} c_i \Phi(\boldsymbol{x}, \boldsymbol{y}_i), \quad \boldsymbol{x} \in D.$$

In numerical experiments, the closed curve S is often chosen as $(1 + \eta)\boldsymbol{z}(t)$, where $\eta > 0$. From the scattered fields u^s measured on curve C, the above undetermined coefficients $c_i, i = 1, \cdots, N$ are solved by

$$\sum_{i=1}^{N} c_i \Phi(\boldsymbol{x}_j, \boldsymbol{y}_i) \approx u^s(\boldsymbol{x}_j), \quad \boldsymbol{x}_j \in C, \ j = 1, \cdots, M.$$

Since the above system of equations is ill-posed, we add regularization to it. Suppose that we have the following least-squares functional:

$$F_\alpha(c_1, \cdots, c_N) = \sum_{j=1}^{M} \left| \sum_{i=1}^{N} c_i \Phi(\boldsymbol{x}_j, \boldsymbol{y}_i) - u^s(\boldsymbol{x}_j) \right|^2 + \alpha \sum_{i=1}^{N} |c_i|^2, \tag{3.6}$$

where α is the regularization parameter, and we obtain the coefficients c_i by minimizing the above least-squares functional $F_\alpha(c_1, \cdots, c_N)$. Then, we have

$$u(\boldsymbol{x}) \approx \sum_{i=1}^{N} c_i \Phi(\boldsymbol{x}, \boldsymbol{y}_i) + u^i(\boldsymbol{x}), \quad \boldsymbol{x} \in \partial D. \tag{3.7}$$

$$\frac{\partial u}{\partial \boldsymbol{\nu}}(\boldsymbol{x}) \approx \sum_{i=1}^{N} c_i \frac{\partial \Phi(\boldsymbol{x}, \boldsymbol{y}_i)}{\partial \boldsymbol{\nu}} + \frac{\partial u^i}{\partial \boldsymbol{\nu}}(\boldsymbol{x}), \quad \boldsymbol{x} \in \partial D. \tag{3.8}$$

Because the fundamental solutions satisfy the Helmholtz equation (2.1), the total field u merely needs to satisfy the general boundary condition $G(u) = 0$ on ∂D.

In the second step, we use the Newton's method to find the boundary curve $\boldsymbol{z}(t)$ that satisfies $G(u) = 0$ on ∂D. Suppose that $\boldsymbol{z}(t) : \mathbb{R} \to \mathbb{R}^2$ is a 2π periodic C^2 continuous function. Given a C^2 continuous function u defined in the neighborhood of ∂D, we denote the general boundary operator

$$\tilde{G}(\boldsymbol{z}) := G(u(\boldsymbol{z})),$$

that is,

$$\tilde{G} : \boldsymbol{z} \mapsto \mathcal{R}\left(\frac{\partial u}{\partial \boldsymbol{\nu}} \circ \boldsymbol{z}\right) \mathcal{R}(u \circ \boldsymbol{z}) + \mathcal{I}\left(\frac{\partial u}{\partial \boldsymbol{\nu}} \circ \boldsymbol{z}\right) \mathcal{I}(u \circ \boldsymbol{z}). \tag{3.9}$$

We use the Newton's method to solve the boundary equation $\tilde{G}(\boldsymbol{z}) = 0$, that is,

$$\tilde{G}(\boldsymbol{z}_n) + \tilde{G}'(\boldsymbol{z}_n)\boldsymbol{h} = 0, \quad \boldsymbol{z}_{n+1} = \boldsymbol{z}_n + \boldsymbol{h}.$$

Here, $\tilde{G}'$ is the Fréchet derivative of $\tilde{G}$, and $\boldsymbol{z}_n(t) = r_n(t)(\cos t, \sin t)$ is the approximation of the cavity boundary in the nth iteration. The parametric form of $r_n(t)$ is as follows:

$$r_n(t) = a_0 + \sum_{j=1}^{N_1} [a_j \cos(jt) + b_j \sin(jt)], \tag{3.10}$$

where N_1 is the truncation term and $r_n(t) > 0$. To solve the Newton's equation, the data u and $\frac{\partial u}{\partial \boldsymbol{\nu}}$ on the approximated cavity boundary can be obtained from the first step. For the new boundary curve $\boldsymbol{z}_{n+1}$, the above two steps are repeated until n reaches the designated maximum number of iteration steps or some stopping criteria are fulfilled.

Finally, we compute the Fréchet derivative $\tilde{G}'(\boldsymbol{z}_n)\boldsymbol{h}$. For convenience, we define

$$\tilde{G}_1 : \boldsymbol{z} \mapsto u \circ \boldsymbol{z}, \quad \tilde{G}_2 : \boldsymbol{z} \mapsto \frac{\partial u}{\partial \boldsymbol{\nu}} \circ \boldsymbol{z}.$$

Thus,

$$\tilde{G}(z) = \mathcal{R}(\tilde{G}_2(z))\mathcal{R}(\tilde{G}_1(z)) + \mathcal{I}(\tilde{G}_2(z))\mathcal{I}(\tilde{G}_1(z)).$$

In the following, we use $\boldsymbol{\tau}$ to denote the unit tangent vector to ∂D. Then, $\boldsymbol{\tau} \circ z = z'/|z'|$ and $\boldsymbol{\nu} \circ z = z'^{\perp}/|z'|$. In the situation without misunderstanding, we still adopt the notations $\boldsymbol{\tau} = \boldsymbol{\tau} \circ z$ and $\boldsymbol{\nu} = \boldsymbol{\nu} \circ z$. In References [25, 27], the authors gave the Fréchet derivatives of $\tilde{G}_1$ and $\tilde{G}_2$, and in Reference [24], the authors summarized the corresponding results in the following two theorems.

Theorem 3. *The operators $\tilde{G}_1$ and $\tilde{G}_2$ from $C^2([0, 2\pi])$ to $C([0, 2\pi])$ are both Fréchet differentiable, and their derivatives are given by*

$$\tilde{G}_1'(z)\boldsymbol{h} = (\nabla u \circ z) \cdot \boldsymbol{h}, \tag{3.11}$$

$$\tilde{G}_2'(z)\boldsymbol{h} = -\frac{\boldsymbol{h}' \cdot \boldsymbol{\nu}}{|z'|}\frac{\partial u}{\partial \boldsymbol{\tau}} \circ z + (\boldsymbol{h} \cdot \boldsymbol{\tau})\left[\frac{\partial^2 u}{\partial \boldsymbol{\tau}\partial \boldsymbol{\nu}} \circ z - H\frac{\partial u}{\partial \boldsymbol{\tau}} \circ z\right] + (\boldsymbol{h} \cdot \boldsymbol{\nu})\frac{\partial^2 u}{\partial \boldsymbol{\nu}^2} \circ z, \tag{3.12}$$

where $H := -\boldsymbol{\nu} \cdot z''/|z'|^2$ stands for the curvature. Provided that the field u satisfies the Helmholtz equation, the Fréchet derivative of $\tilde{G}_2'$ is simplified as

$$\begin{aligned}\tilde{G}_2'(z)\boldsymbol{h} =& -k^2(\boldsymbol{h} \cdot \boldsymbol{\nu})u \circ z - \frac{\partial}{\partial \boldsymbol{\tau}}\left(\boldsymbol{h} \cdot \boldsymbol{\nu}\left(\frac{\partial u}{\partial \boldsymbol{\tau}} \circ z\right)\right) \\ &+ H(\boldsymbol{h} \cdot \boldsymbol{\nu})\frac{\partial u}{\partial \boldsymbol{\nu}} \circ z + (\boldsymbol{h} \cdot \boldsymbol{\tau})\frac{\partial^2 u}{\partial \boldsymbol{\tau}\partial \boldsymbol{\nu}} \circ z.\end{aligned} \tag{3.13}$$

By use of the above theorem, we obtain the following theorem.

Theorem 4. *$\tilde{G} : C^2[0, 2\pi] \mapsto C[0, 2\pi]$ is Fréchet differentiable, and its derivative is given by*

$$\begin{aligned}\tilde{G}'(z)\boldsymbol{h} =& \mathcal{R}(\tilde{G}_1(z))(\mathcal{R}(\tilde{G}_2(z)))'\boldsymbol{h} + \mathcal{R}(\tilde{G}_2(z))(\mathcal{R}(\tilde{G}_1(z)))'\boldsymbol{h} \\ &+ \mathcal{I}(\tilde{G}_1(z))(\mathcal{I}(\tilde{G}_2(z)))'\boldsymbol{h} + \mathcal{I}(\tilde{G}_2(z))(\mathcal{I}(\tilde{G}_1(z)))'\boldsymbol{h},\end{aligned} \tag{3.14}$$

where the Fréchet derivatives $(\mathcal{R}(\tilde{G}_1(z)))'\boldsymbol{h}$ and $(\mathcal{I}(\tilde{G}_1(z)))'\boldsymbol{h}$ can be achieved from (3.11) by taking the real part or the imaginary part of u, and the Fréchet derivatives $(\mathcal{R}(\tilde{G}_2(z)))'\boldsymbol{h}$ and $(\mathcal{I}(\tilde{G}_2(z)))'\boldsymbol{h}$ can be achieved from (3.12) by taking the real part or the imaginary part of u. If u satisfies the Helmholtz equation, $(\mathcal{R}(\tilde{G}_2(z)))'\boldsymbol{h}$ and $(\mathcal{I}(\tilde{G}_2(z)))'\boldsymbol{h}$ can also be simplified by (3.13).

4. Numerical examples

In this section, we present three numerical examples corresponding to the three types of boundary conditions. Throughout this section, we assume the incident wave $u^i = \Phi(\boldsymbol{x}, \boldsymbol{d}) = \frac{\mathrm{i}}{4}H_0^{(1)}(k|\boldsymbol{x} - \boldsymbol{d}|)$, $k = 1$, and $\boldsymbol{d}$ is the position of the source point. The number of scattered fields measured on a circle C is $M = 128$. The number of source points is $N = 128$ on a closed curve S_n with $(1 + \eta)z_n(t)$, where $\eta = 0.1$. We use the integral equation method in [3, 9] to obtain the exact measured data u^s on C. To test the stability of the hybrid method, we add some random noise to the exact scattered field u^s by

$$u^{s,\delta} = u^s + \delta r_1|u^s|e^{\mathrm{i}\pi r_2},$$

where r_1 and r_2 are two random numbers uniformly distributed in $[-1, 1]$, and $\delta > 0$ is the relative noise level. In the following examples, we mainly consider $\delta = 1\%$ and $\delta = 5\%$.

In the computation, we recall the approximation of the cavity boundary $z_n(t) = r_n(t)(\cos t, \sin t)$ in the nth iteration and the parametric form of $r_n(t)$ is described in (3.10). For the boundary z_n, we first compute the coefficients c_j by solving the least-squares problem (3.6), and then we obtain the total field u and its derivative $\frac{\partial u}{\partial \nu}$ from (3.7) and (3.8), respectively.

In the second step of the hybrid method, the iteration step is defined as

$$\boldsymbol{h}(t) = \left(a_0^{(h)} + \sum_{j=1}^{N_1} [a_j^{(h)} \cos(jt) + b_j^{(h)} \sin(jt)] \right) (\cos t, \sin t).$$

Choosing some discrete points $t_i, i = 1, \cdots, 512$ in $[0, 2\pi]$, we obtain the discretization of the Newton's equation $\tilde{G}(z_n) + \tilde{G}'(z_n)\boldsymbol{h} = 0$, where $\tilde{G}(z_n)$ is computed by (3.9) and $\tilde{G}'(z_n)\boldsymbol{h}$ is computed by (3.14). The following equation is also needed for the computation of (3.11):

$$\nabla u = \boldsymbol{\nu} \frac{\partial u}{\partial \boldsymbol{\nu}} + \boldsymbol{\tau} \frac{\partial u}{\partial \boldsymbol{\tau}}, \quad \boldsymbol{x} \in \partial D_n.$$

We choose the stopping criterion as follows:

$$\|\tilde{G}(z_n) - \tilde{G}(z_{n-1})\| < 10^{-2}.$$

Example 1. In this example, we consider an interior inverse scattering problem with the Dirichlet boundary condition. We first consider a triangular cavity with the following parametric form:

$$z(t) = (1 + 0.2 \cos 3t)(\cos t, \sin t), \quad t \in [0, 2\pi] \tag{4.1}$$

In the experiment, we choose $\boldsymbol{d} = (0.5, 0)$ as the source point, the radius r_c of the measured curve C is 0.5 and the number of terms in the parametric form $r_n(t)$ is $N_1 = 3$. We set the initial boundary as a circle with a radius of 0.7. Therefore, the initial value of $[a_0, a_1, a_2, a_3, b_1, b_2, b_3]$ is $[0.7, 0, 0, 0, 0, 0, 0]$. The reconstruction of the cavity without noise is shown in Figure 2. The green line in Figure 2 is the initial guess of the cavity boundary, the blue line is the exact cavity boundary and the red dotted line is the reconstruction of the cavity boundary. From this figure, we can see that the reconstruction is almost exact without noise, and the computational time is short (1.5 s on a laptop with an Intel Core i7 processor at 2.5 GHz and 12 GB of RAM).

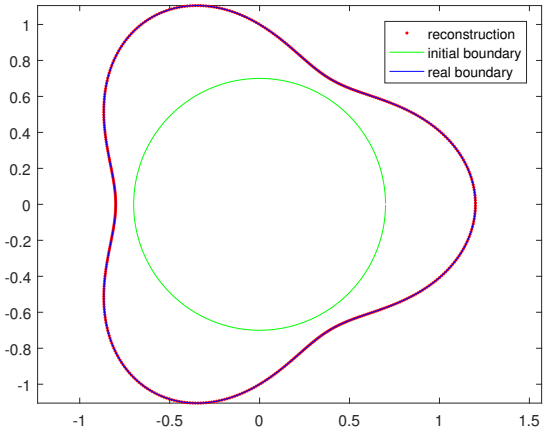

Figure 2. Reconstruction of a cavity without noise for the Dirichlet case.

When the noise level is 1%, we choose the regularization parameter $\alpha = 10^{-3}$, and when the noise level is 5%, we choose the regularization parameter $\alpha = 10^{-2}$. The reconstructions of the cavity with different noise levels are presented in Figure 3. This experiment shows that the hybrid method is effective for cases with different noise levels under the Dirichlet boundary condition.

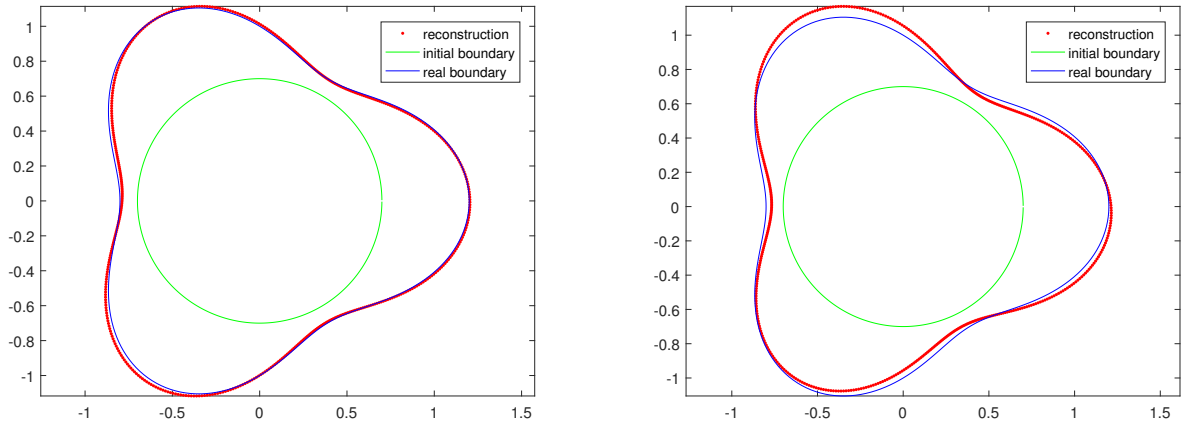

Figure 3. Reconstructions of the cavity with 1% noise (left) and 5% noise (right) for the Dirichlet case, ($r_c = 0.5$).

Now, we choose a different radius $r_c = 0.3$ for the measured curve C and the source point at $\boldsymbol{d} = (0.3, 0)$. The regularization parameter $\alpha = 10^{-3}$ when the noise level is 1%, and $\alpha = 8 \times 10^{-3}$ when the noise level is 5%. The other parameters are the same as above. The reconstructions of the cavity are shown in Figure 4. Compared with Figure 3 in the above experiment, we can see that the reconstruction is affected by the distance between the measured curve and the cavity boundary. When the distance is larger, the reconstruction is worse than that in Figure 3.

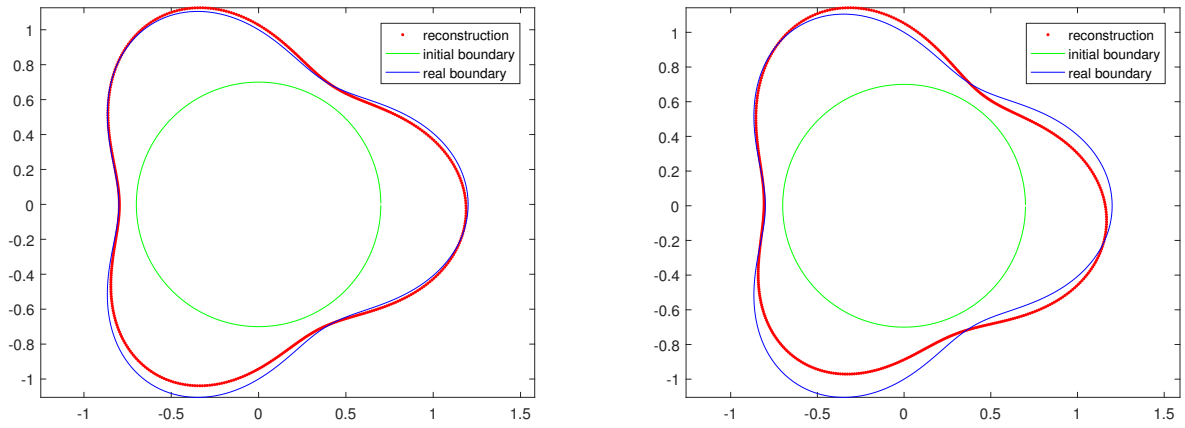

Figure 4. Reconstructions of the cavity with 1% noise (left) and 5% noise (right) for the Dirichlet case, ($r_c = 0.3$).

In the experiments conducted throughout Section 4, we choose the number of source points $N = 128$

and the regularization parameter α by trial and error. In the following experiment, we consider the effects of different choices for these two parameters on the resulting numerical performance. First, we define the relative error between the numerical solution $r_n(t)$ and the exact solution $r(t)$ as follows:

$$\frac{\|r(t) - r_n(t)\|_2}{\|r(t)\|_2}.$$

From the expression of the triangular domain (4.1), $r(t) = 1 + 0.2\cos 3t$. Then, we present the relative errors with different regularization parameters α in the left subfigure of Figure 5. The noise level is 1%, and the other parameters are the same as those used in the first experiment in Example 1. This figure illustrates that the relative error declines with increasing α and then increases. The best interval of α is approximately 9×10^{-5} to 5×10^{-3}.

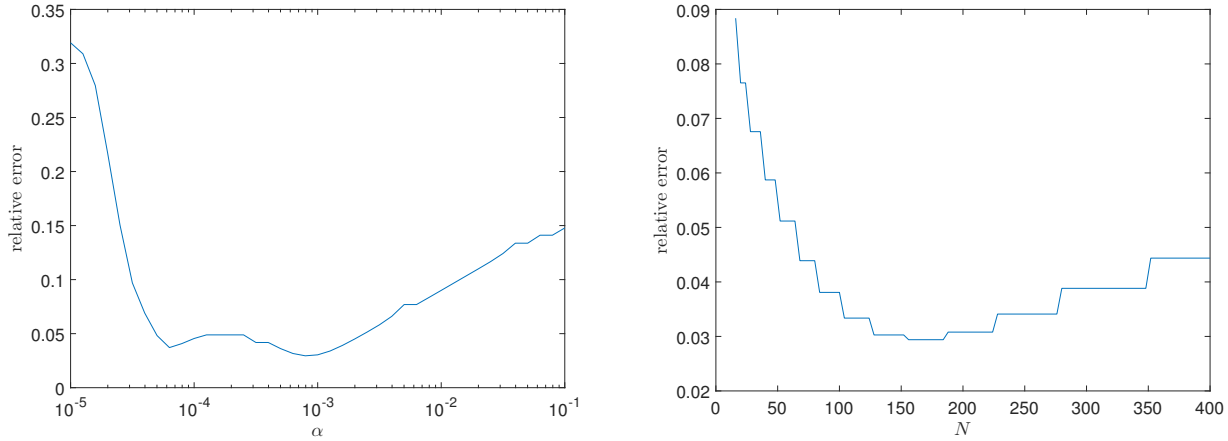

Figure 5. Relative errors with increasing α (left) and relative errors with increasing N (right).

Second, we consider the relative errors with different values of N. In this experiment, the noise level is 1%, the regularization parameter $\alpha = 10^{-3}$ and the other parameters are the same as those in the first experiment in Example 1. From the right subfigure of Figure 5, the relative error also declines as N increases and then increases. The best interval of N is about 100–225. This figure also shows that the relative error does not decrease when N is sufficiently large. The effect of N on the numerical performance is somewhat similar to that of the regularization parameter α.

Next, we consider a peanut cavity in the parametric form shown below:

$$z(t) = 2\sqrt{\cos^2 t + 0.25\sin^2 t}(\cos t, \sin t), \quad t \in [0, 2\pi]. \tag{4.2}$$

The source point is at $\boldsymbol{d} = (0.8, 0)$, the radius of C is 0.8 and the number of terms in the parametric form $r_n(t)$ is $N_1 = 5$. The initial value is $[1, 0, 0, 0, 0, 0, 0, 0, 0, 0, 0]$. The reconstruction of the cavity without noise is shown in Figure 6.

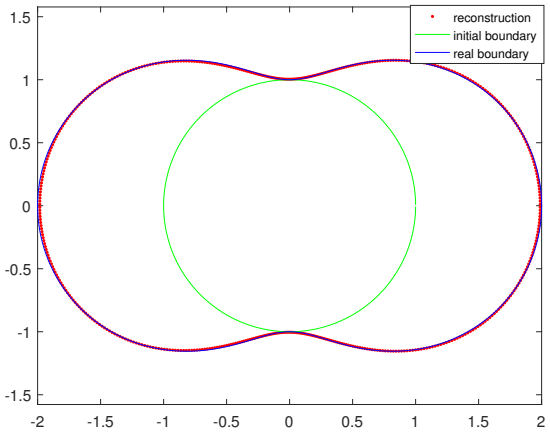

Figure 6. Reconstruction of a cavity without noise for the Dirichlet case.

When the noise level is 1%, we choose the regularization parameter $\alpha = 5 \times 10^{-3}$, and when the noise level is 5%, we choose $\alpha = 10^{-2}$. The reconstructions of the cavity with different noise levels are presented in Figure 7. From this experiment, we can see that the hybrid method is also effective for the peanut cavity.

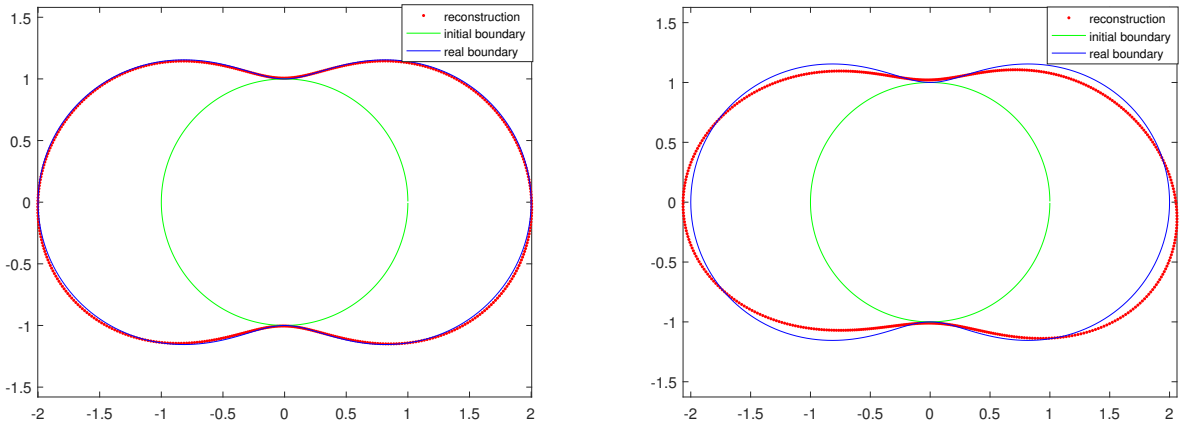

Figure 7. Reconstructions of the cavity with 1% noise (left) and 5% noise (right) for the Dirichlet case.

Example 2. In this example we consider the interior inverse scattering problem with the Neumann boundary condition. First, we present the triangular case with the same parametric form of (4.1) in Example 1. In the experiment, we choose the source point at $\boldsymbol{d} = (0.5, 0)$, the radius of C is 0.5 and the number of terms in the parametric form $r_n(t)$ is $N_1 = 3$. The initial boundary is a circle with a radius of 0.7. Therefore, the initial value of $[a_0, a_1, a_2, a_3, b_1, b_2, b_3]$ is $[0.7, 0, 0, 0, 0, 0, 0]$. The reconstruction of the cavity without noise is shown in Figure 8. From this figure, we can see that the reconstruction is also effective with the Neumann boundary condition.

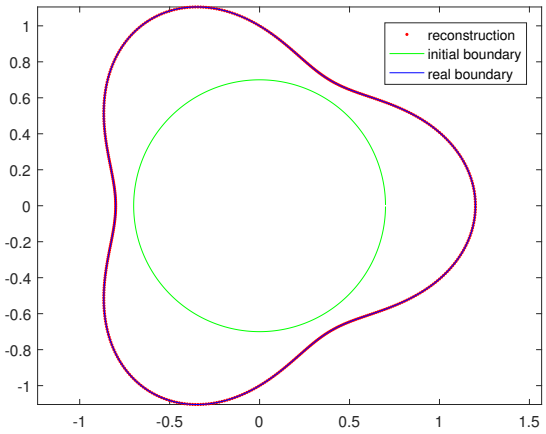

Figure 8. Reconstruction of the cavity without noise for the Neumann case.

When the noise level is 1%, we choose the regularization parameter $\alpha = 5 \times 10^{-3}$, and when the noise level is 5%, we choose $\alpha = 4 \times 10^{-2}$. The reconstructions of the cavity with different noise levels are presented in Figure 9. This experiment shows that the inversion effect with the Neumann boundary condition is sensitive to the noise level. When the noise level is high, the reconstruction is not very good.

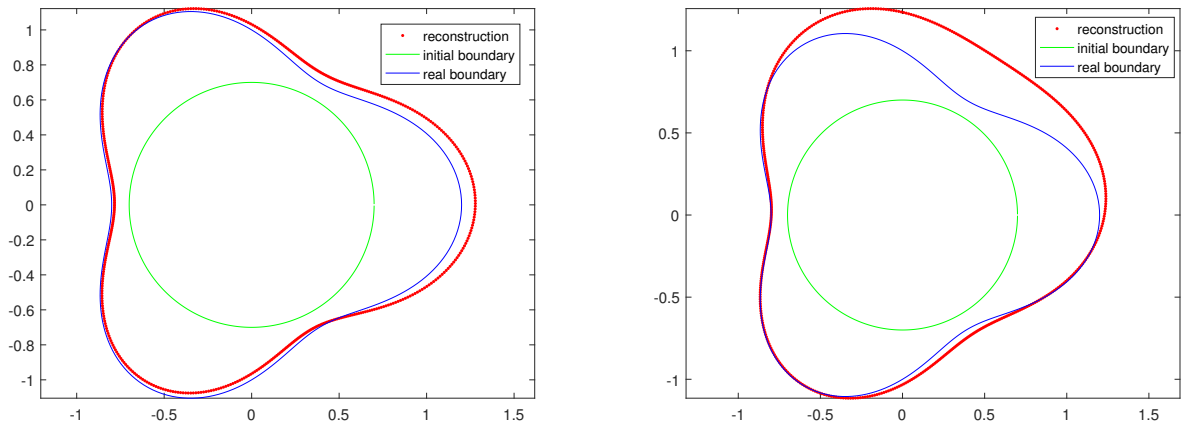

Figure 9. Reconstructions of the cavity with 1% noise (left) and 5% noise (right) for the Neumann case, ($r_c = 0.5$).

Now, we choose a different radius $r_c = 0.6$ for the measured curve C and select the source point at $\boldsymbol{d} = (0.6, 0)$. The regularization parameter $\alpha = 10^{-2}$ when the noise level is 1%, and $\alpha = 8 \times 10^{-1}$ when the noise level is 5%. The other parameters are the same as above. The reconstructions of the cavity are shown in Figure 10. Compared with Figure 9 in the above experiment, we can see that, under the Neumann boundary condition, the reconstruction is also affected by the distance between the measured curve and the cavity boundary. When the distance is smaller, the reconstruction is better.

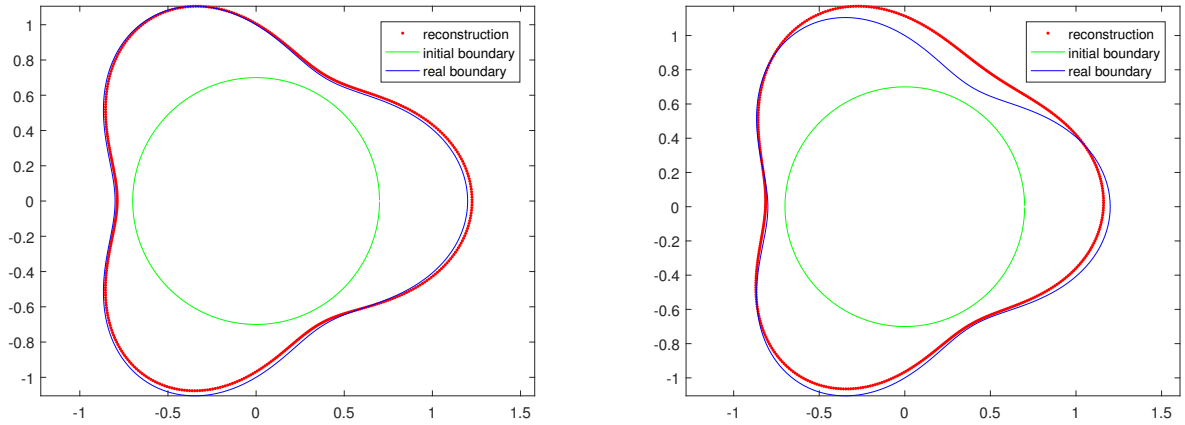

Figure 10. Reconstructions of the cavity with 1% noise (left) and 5% noise (right) for the Neumann case, ($r_c = 0.6$).

Next, we consider a peanut cavity with the same parametric form (4.2) as that in Example 1. The source point is at $\boldsymbol{d} = (0, 0.6)$, the radius of C is 0.6 and the number of terms in the parametric form $r_n(t)$ is $N_1 = 5$. The initial value is $[1.2, 0, 0, 0, 0, 0, 0, 0, 0, 0, 0]$. The reconstruction of the cavity without noise is shown in Figure 11.

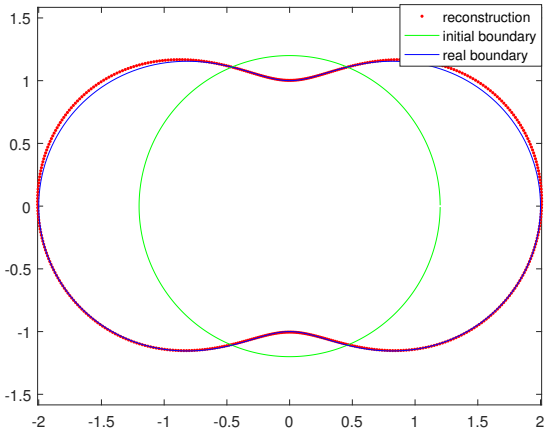

Figure 11. Reconstruction of the cavity without noise for the Neumann case.

When the noise level is 1%, we choose the regularization parameter $\alpha = 10^{-3}$, and when the noise level is 5%, we choose $\alpha = 2 \times 10^{-2}$. The reconstructions of the cavity with different noise levels are presented in Figure 12.

Example 3. In this example, we consider the interior inverse scattering problem with the impedance boundary condition. We reconstruct the shape of the cavity and the impedance function λ simultaneously, where λ is approximated by (3.4). First, we present the triangular case with the same parametric form of (4.1) as that in Example 1. In the experiment, we choose the source point at $\boldsymbol{d} = (0.7, 0)$, the radius r_c of the measured curve C is 0.7 and the number of terms in the parametric form $r_n(t)$ is $N_1 = 3$. The initial boundary is a circle with a radius of 1.5, that is, the initial value of $[a_0, a_1, a_2, a_3, b_1, b_2, b_3]$

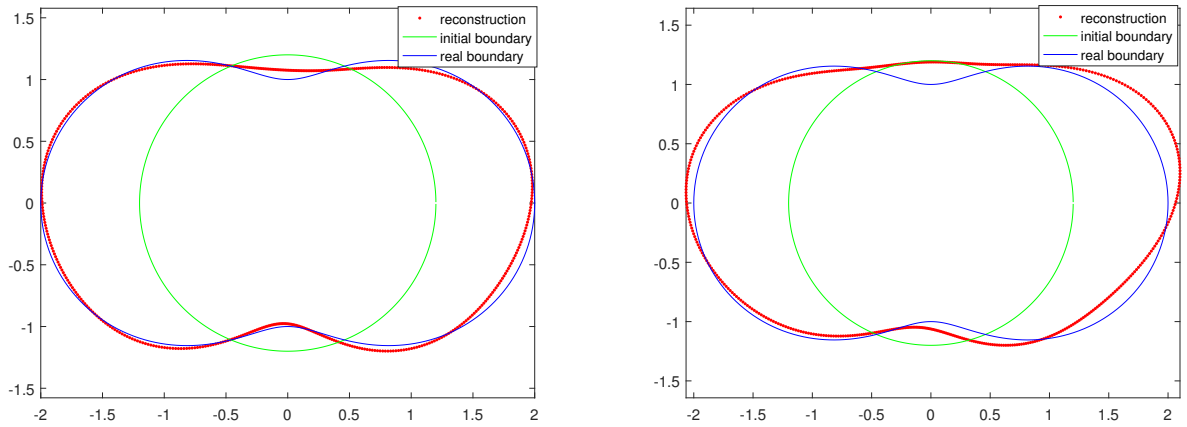

Figure 12. Reconstructions of the cavity with 1% noise (left) and 5% noise (right) for the Neumann case.

is $[1.5, 0, 0, 0, 0, 0, 0]$. The exact impedance function λ is given in the following form:

$$\lambda = 1 + \sin^3(t), \quad t \in [0, 2\pi]. \tag{4.3}$$

The reconstructions of the cavity boundary and the impedance function λ without noise are shown in Figure 13. The green line in the left subfigure of Figure 13 is the initial guess of the cavity boundary, the blue line is the exact cavity boundary and the red dotted line is the reconstruction of the cavity boundary. The blue line in the right subfigure of Figure 13 is the exact impedance function, and the red line is the reconstruction of the impedance function. Figure 13 shows that the hybrid method is effective with the impedance boundary condition.

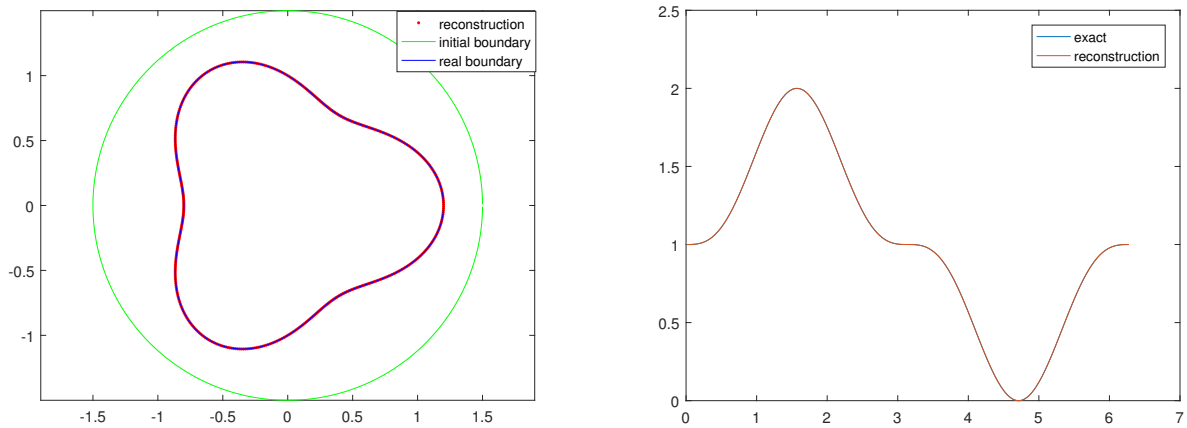

Figure 13. Reconstructions of the cavity (left) and the impedance function (right), without noise, ($r_c = 0.7$).

When the noise level is 1%, we choose the regularization parameter $\alpha = 2 \times 10^{-2}$, and when the noise level is 5%, we choose $\alpha = 1 \times 10^{-1}$. The reconstructions of the cavity and the impedance function with 1% noise are presented in Figure 14, and the reconstructions obtained with 5% noise are

presented in Figure 15. From Figures 14 and 15, the reconstruction of the impedance function λ is obviously affected by the noise level.

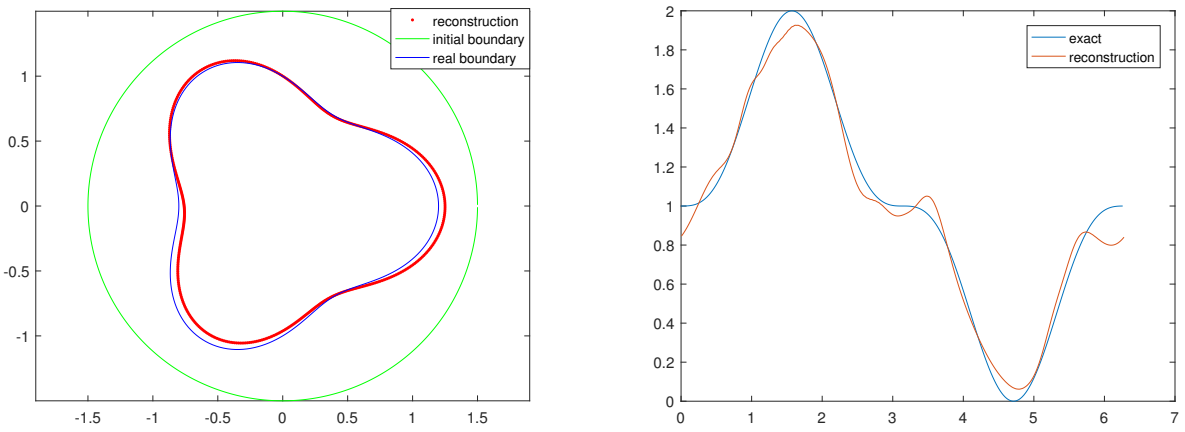

Figure 14. Reconstructions of the cavity (left) and the impedance function (right), with 1% noise, ($r_c = 0.7$).

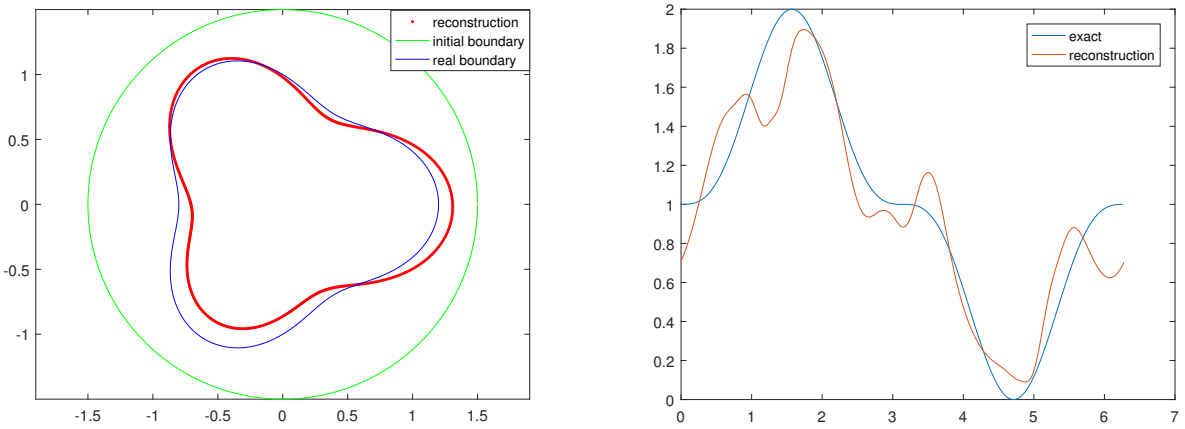

Figure 15. Reconstructions of the cavity (left) and the impedance function (right), with 5% noise, ($r_c = 0.7$).

In the next experiment, we choose the source point at $\boldsymbol{d} = (0.5, 0)$, and the radius r_c of the measured curve C is 0.5. The other parameters are the same as those in the above experiment. The regularization parameter $\alpha = 3 \times 10^{-3}$ with 1% noise and $\alpha = 10^{-1}$ with 5% noise. The reconstructions are presented in Figures 16 and 17. Comparing Figures 14 and 15 with Figures 16 and 17, we can see that the reconstruction is also affected by the distance between the measured curve and the cavity boundary. This is consistent with the linear sampling method described in Reference [5] and the direct imaging method utilized in [16] for the interior inverse scattering problem.

Finally, we consider another impedance function given by

$$\lambda = 1 - \cos(t) + 0.5 * \sin(2t), \quad t \in [0, 2\pi]. \tag{4.4}$$

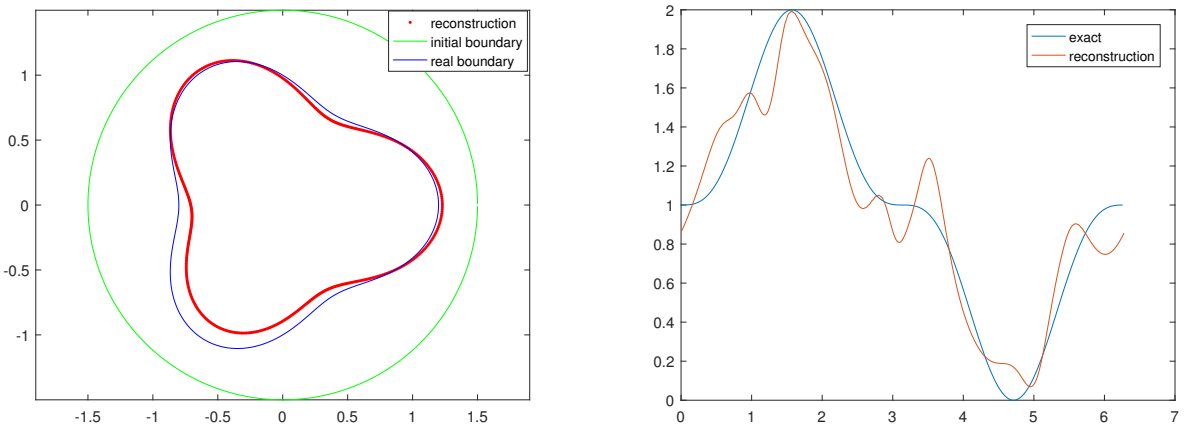

Figure 16. Reconstructions of the cavity (left) and the impedance function (right), with 1% noise, ($r_c = 0.5$).

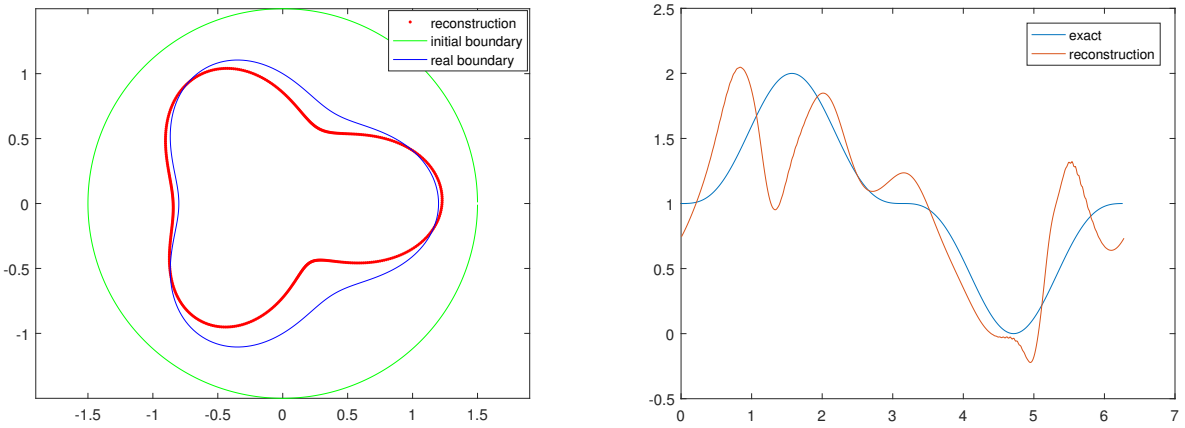

Figure 17. Reconstructions of the cavity (left) and the impedance function (right), with 5% noise, ($r_c = 0.5$).

In this experiment, we choose the source point at $\boldsymbol{d} = (0.7, 0)$, $r_c = 0.7$ and the number of terms in the parametric form $r_n(t)$ is $N_1 = 3$. The initial value is the same as above. The reconstructions of the cavity boundary and the impedance function λ without noise are shown in Figure 18.

When the noise level is 1%, we choose the regularization parameter $\alpha = 2\times10^{-2}$, and when the noise level is 5%, we choose $\alpha = 10^{-1}$. The reconstructions of the cavity and the impedance function with 1% noise are presented in Figure 19, and the reconstructions obtained with 5% noise are presented in Figure 20. From this experiment, we can see that the hybrid method is effective with different impedance functions.

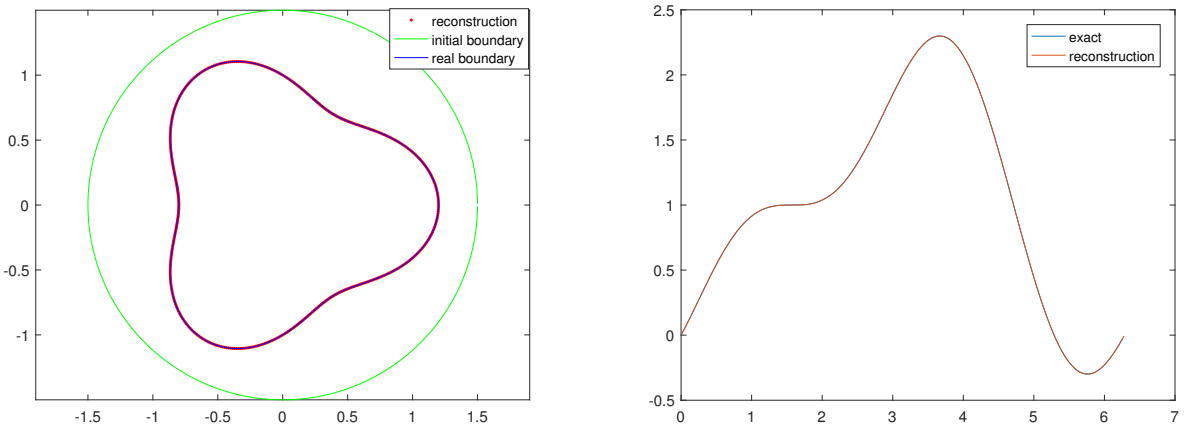

Figure 18. Reconstructions of the cavity (left) and the impedance function (right), without noise, ($r_c = 0.7$).

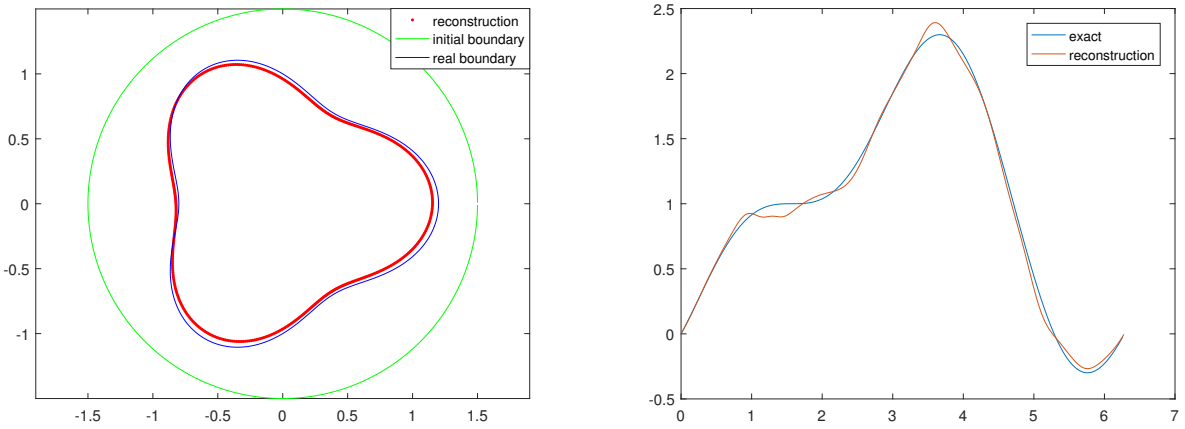

Figure 19. Reconstructions of the cavity (left) and the impedance function (right), with 1% noise, ($r_c = 0.7$).

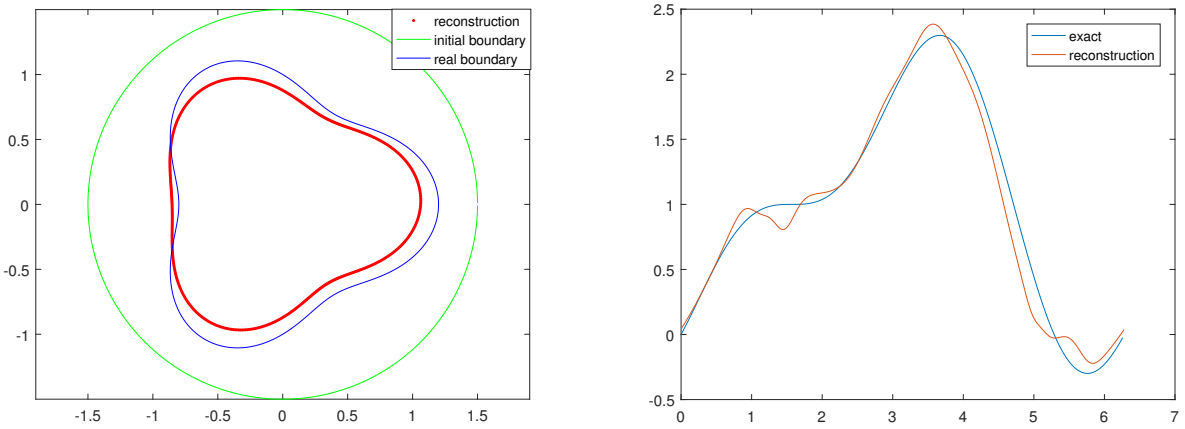

Figure 20. Reconstructions of the cavity (left) and the impedance function (right), with 5% noise, ($r_c = 0.7$).

Finally, we provide some comments about the performance of the method with different initial values. Like most Newton's methods, our method only exhibits local convergence. When the initial value is close to the exact boundary, the numerical solution converges to the exact solution quickly. We can obtain the desired reconstruction after 15–30 iterations. However, if the initial guess is not close to the exact boundary, the numerical solution does not converge or may converge to somewhere else. Therefore, the reconstruction is far away from the exact boundary.

5. Conclusions

In this paper, we studied a hybrid method for the interior inverse scattering problem. The MFS is employed instead of the integral equation method in the first step of the hybrid method. Through the use of the general boundary condition, we can reconstruct the shape of a cavity without prior information about the boundary condition type. Numerical examples show that our method is effective. However, when the noise level is high, the reconstructions are not very good for the impedance boundary condition. In the future, we will try to improve the method or the general boundary condition to obtain a better inversion effect. We will also consider this hybrid method for different inverse scattering problems, e.g., inverse problems with periodic structures.

Acknowledgments

The authors would like to thank the editors and the reviewers for their careful reading and valuable comments, which have improved the quality of the original submitted manuscript. The authors also acknowledge the support of project 12271482 and project 11626054 of the National Natural Science Foundation of China.

Conflict of interest

The authors declare that there are no conflicts of interest.

References

1. D. Colton, R. Kress, *Inverse Acoustic and Electromagnetic Scattering Theory*, 4th edition, Springer, Berlin, 2019. https://doi.org/10.1007/978-3-030-30351-8
2. F. Cakoni, D. Colton, *Qualitative Methods in Inverse Scattering Theory*, Springer, Berlin, 2006. https://doi.org/10.1007/3-540-31230-7
3. D. Colton, R. Kress, *Integral Equation Methods in Scattering Theory*, Wiley, Chichester, 1983. https://doi.org/10.1137/1.9781611973167
4. P. Jakubik, R. Potthast, Testing the integrity of some cavity—the Cauchy problem and the range test, *Appl. Numer. Math.*, **58** (2008), 899–914. https://doi.org/10.1016/j.apnum.2007.04.007
5. H. Qin, D. Colton, The inverse scattering problem for cavities, *Appl. Numer. Math.*, **62** (2012), 699–708. https://doi.org/10.1016/j.apnum.2010.10.011
6. H. Qin, D. Colton, The inverse scattering problem for cavities with impedance boundary condition, *Adv. Comput. Math.*, **36** (2012), 157–174. https://doi.org/10.1007/s10444-011-9179-2

7. F. Zeng, F. Cakoni, J. Sun, An inverse electromagnetic scattering problem for a cavity, *Inverse Probl.*, **27** (2011), 125002. https://doi.org/10.1088/0266-5611/27/12/125002
8. F. Zeng, S. Meng, The interior inverse electromagnetic scattering for an inhomogeneous cavity, *Inverse Probl.*, **37** (2021), 025007. https://doi.org/10.1088/1361-6420/abd7cc
9. H. Qin, F. Cakoni, Nonlinear integral equations for shape reconstruction in the inverse interior scattering problem, *Inverse Probl.*, **27** (2011), 035005. https://doi.org/10.1088/0266-5611/27/3/035005
10. F. Zeng, P. Suarez, J. Sun, A decomposition method for an interior inverse scattering problem, *Inverse Probl. Imaging*, **7** (2013), 291–303. https://doi.org/10.3934/ipi.2013.7.291
11. L. Liu, J. Cai, Y. Xu, Regularized Newton iteration method for a penetrable cavity with internal measurements in inverse scattering problem, *Math. Methods Appl. Sci.*, **43** (2019), 2665–2678. https://doi.org/10.1002/mma.6074
12. X. Liu, The factorization method for cavities, *Inverse Probl.*, **30** (2014), 015006. https://doi.org/10.1088/0266-5611/30/1/015006
13. F. Qu, J. Yang, H. Zhang, Shape reconstruction in inverse scattering by an inhomogeneous cavity with internal measurements, *SIAM J. Imag. Sci.*, **12** (2019), 788–808. https://doi.org/10.1137/18M1232401
14. Y. Wang, F. Ma, E. Zheng, Bayesian method for shape reconstruction in the inverse interior scattering problem, *Math. Probl. Eng.*, **2015** (2015), 1–12. https://doi.org/10.1155/2015/935294
15. Y. Sun, Y. Guo, F. Ma, The reciprocity gap functional method for the inverse scattering problem for cavities, *Appl. Anal.*, **95** (2016), 1327–1346. https://doi.org/10.1080/00036811.2015.1064519
16. D. Zhang, Y. Wu, Y. Wang, Y. Guo, A direct imaging method for the exterior and interior inverse scattering problems, *Inverse Probl. Imaging*, **16** (2022), 1299–1323. https://doi.org/10.3934/ipi.2022025
17. Y. Yin, W. Yin, P. Meng, H. Liu, The interior inverse scattering problem for a two-layered cavity using the Bayesian method, *Inverse Probl. Imaging*, **16** (2022), 673–690. https://doi.org/10.3934/ipi.2021069
18. Y. Ou, F. Zeng, An interior inverse scattering problem in elasticity, *Appl. Anal.*, **101** (2022), 796–809. https://doi.org/10.1080/00036811.2020.1758312
19. Y. Hu, F. Cakoni, J. Liu, The inverse scattering problem for a partially coated cavity with interior measurements, *Appli. Anal.*, **93** (2014), 936–956. https://doi.org/10.1080/00036811.2013.801458
20. L. Liu, The inverse scattering problem for a partially coated penetrable cavity with interior measurements, *Appl. Anal.*, **96** (2017), 844–868. https://doi.org/10.1080/00036811.2016.1160073
21. Y. Gao, H. Liu, X. Wang, K. Zhang, On an artificial neural network for inverse scattering problems, *J. Comput. Phys.*, **448** (2022), 110771. https://doi.org/10.1016/j.jcp.2021.110771
22. W. Yin, W. Yang, H. Liu, A neural network scheme for recovering scattering obstacles with limited phaseless far-field data, *J. Comput. Phys.*, **417** (2020), 109594. https://doi.org/10.1016/j.jcp.2020.109594

23. W. Yin, J. Ge, P. Meng, F. Qu, A neural network method for the inverse scattering problem of impenetrable cavities, *Electron. Res. Arch.*, **28** (2020), 1123–1142. https://doi.org/10.3934/era.2020062

24. J. Liu, F. Ma, An improved hybrid method for inverse obstacle scattering problems, *Commun. Math. Res.*, **27** (2011), 215–226. https://doi.org/10.13447/j.1674-5647.2011.03.010

25. R. Kress, P. Serranho, A hybrid method for sound-hard obstacle reconstruction, *J. Comput. Appl. Math.*, **204** (2007), 418–427. https://doi.org/10.1016/j.cam.2006.02.047

26. P. Serranho, A hybrid method for inverse scattering for shape and impedance, *Inverse Probl.*, **22** (2006), 663–680. https://doi.org/10.1088/0266-5611/22/2/017

27. P. Serranho, *A hybrid method for inverse obstacle scattering problems*, Ph.D thesis, Georg-August-Universität, Germany, Göttingen, 2007. https://doi.org/11858/00-1735-0000-0006-B38F-0

28. R. Kress, Uniqueness and numerical methods in inverse obstacle scattering, *J. Phys. Conf. Ser.*, **73** (2007), 012003. https://doi.org/10.1088/1742-6596/73/1/012003

AIMS Press